



Effects of Si addition on glass-forming ability and crystallization behavior of DyCoAl bulk metallic glass



Liliang Shao^a, Lin Xue^a, Qianqian Wang^a, Kaili Ma^a, Jindu Huang^a, Baolong Shen^{a,b,*}

^a School of Materials Science and Engineering, Jiangsu Key Laboratory of Advanced Metallic Materials, Southeast University, Nanjing 211189, China

^b Institute of Massive Amorphous Metal Science, China University of Mining and Technology, Xuzhou 221116, China

ARTICLE INFO

Article history:

Received 19 September 2020

Received in revised form 18 January 2021

Accepted 9 April 2021

Available online 15 April 2021

Keywords:

Microalloying

Glass-forming ability

Crystallization

Thermodynamics

Kinetics

ABSTRACT

In this work, the glass-forming ability of DyCoAl bulk metallic glass (BMG) was improved by microalloying Si element. Centimeter-level Dy-based BMG was prepared with the addition of 1 at% Si at the expense of Al element. Distinctions of crystallization behavior induced by Si addition for the Dy₅₅Co₂₀Al₂₅ BMG were investigated in terms of isochronal and isothermal crystallization as well as time dependent crystallization. Compared with the Dy₅₅Co₂₀Al₂₅ BMG, the nucleation process changes to a suppressed nucleation with 1 at% Si addition, and then to an explosive nucleation with 3 at% Si addition accompanying the precipitation of Si-containing phases. Meanwhile, the growth of crystalline particle is sluggish for Dy₅₅Co₂₀Al₂₄Si₁ BMG whereas turns to rapid for Dy₅₅Co₂₀Al₂₂Si₃ BMG. These distinctions of crystallization behavior are attributed to the interplay of driving force for crystallization and kinetic fragility of supercooled liquid. This work provides guidance to modulate the magnetocaloric effect of Dy-based BMGs through crystallization treatment.

© 2021 Elsevier B.V. All rights reserved.

1. Introduction

Ferromagnetic materials show a magnetocaloric effect (MCE) near their Curie temperature (T_C) due to the strong dependence of magnetic spin order on an applied magnetic field, which is the base of magnetic refrigeration [1–4]. Among them, heavy rare-earth (HRE)-based metallic glasses (MGs) have attracted extensive scientific interest because of their good magnetocaloric properties [5–9]. Owing to the intrinsic amorphous structure and the second-order magnetic transition, HRE-based MGs usually show a broad temperature range of MCE accompanying high resistance and low hysteresis [10,11], which is favorable for using as magnetic refrigerants. However, the relatively low values of T_C and magnetic entropy change (ΔS_M) of HRE-based MGs limit their applications.

It has been reported that the MCE of MG can be modulated by crystallization treatment [12,13]. High Gd content GdFeAl amorphous/nanocrystalline ribbons with enhanced T_C and refrigeration capacity were prepared through the in-situ precipitation of crystalline Gd phase in the amorphous matrix [14,15]. The whole

crystallization sequences of Gd₆₅Fe₂₅Zn₁₀ amorphous ribbon were clarified from α -Gd phase to GdFe₂ phase then GdZn phase [16]. Compared with the amorphous ribbon, both the T_C and ΔS_M are enhanced through annealing at the temperature above the second crystallization peak. However, the crystallization behavior of quaternary Tb₄₆Y₁₀Co₂₀Al₂₄ bulk metallic glass (BMG) is much more complex [17]. Several crystalline phases such as Al₂Tb precipitate when annealing the BMG in supercooled liquid region (SCLR). After the sample is fully crystallized, the kinds of crystalline phases are too much to be identified totally. The maximum value of ΔS_M for the fully crystallized sample decreases but exhibits a table-like feature. Similar table-like MCE was also reported in a GdCoAl composite with multi-phase structure [18]. Therefore, the investigation of crystallization behavior is of benefit to guiding the modulation of MCE for magnetocaloric MGs. However, the crystallization process of Dy-based MGs has not been studied.

In addition, the glass-forming ability (GFA) of most HRE-based BMGs are less than 3 mm [6], which also limits their further investigation and application. A partial substitution of RE elements by Y element in RE-TM-Al (TM = Fe, Co, Ni) is often used to improve GFA in some alloy systems, such as Er₃₆Y₂₀Co₂₀Al₂₄ (the critical diameter d_c is 12 mm) [19], but the magnetocaloric properties is altered because of the large amount addition of non-magnetic Y element. Substitution of Co by Fe element was also reported to enhance the GFA of a Gd-based BMG, whereas the increasement is limited and

* Corresponding author at: School of Materials Science and Engineering, Jiangsu Key Laboratory of Advanced Metallic Materials, Southeast University, Nanjing 211189, China.

E-mail address: blshen@seu.edu.cn (B. Shen).

ΔS_M decreases [20]. Minor addition of elements that can introduce large negative enthalpy of mixing and atomic size mismatch is effective to improve the GFA of BMGs without deteriorating their functional properties [21,22]. Owing to the small atomic radius and large negative enthalpy of mixing between Si and HRE elements [23], it can be expected to improve the GFA of HRE-based BMGs through microalloying Si element, such as Dy-based BMGs. Besides, microalloying can change the liquid dynamics and microstructures of glass formers. For example, minor Y addition weakens the viscosity discontinuity in Fe-based metallic melts, i.e., reduces the strength of liquid-liquid transition [24]. The cluster symmetry of CeCuAl BMG is modified by minor Co addition [25], and minor Gd

addition increases and stabilizes the solute-centered clusters of CuZrAl BMG [26]. It is noteworthy that microalloying Y element enhances the number of local crystal-like structure for CuZrAl BMG and increases its incubation time [27]. The changes of dynamics and microstructures are perceived to affect the crystallization behaviors of BMGs. However, the effect of microalloying on the crystallization behavior in HRE-based BMGs has not been studied systematically.

This work is devoted to improving the GFA of Dy-based magneto-caloric BMGs through microalloying Si element and investigating the distinction of crystallization behavior induced by Si addition. Centimeter-level Dy-based BMG was prepared with 1 at% Si addition. The crystalline phases were analyzed via isochronal annealing at the

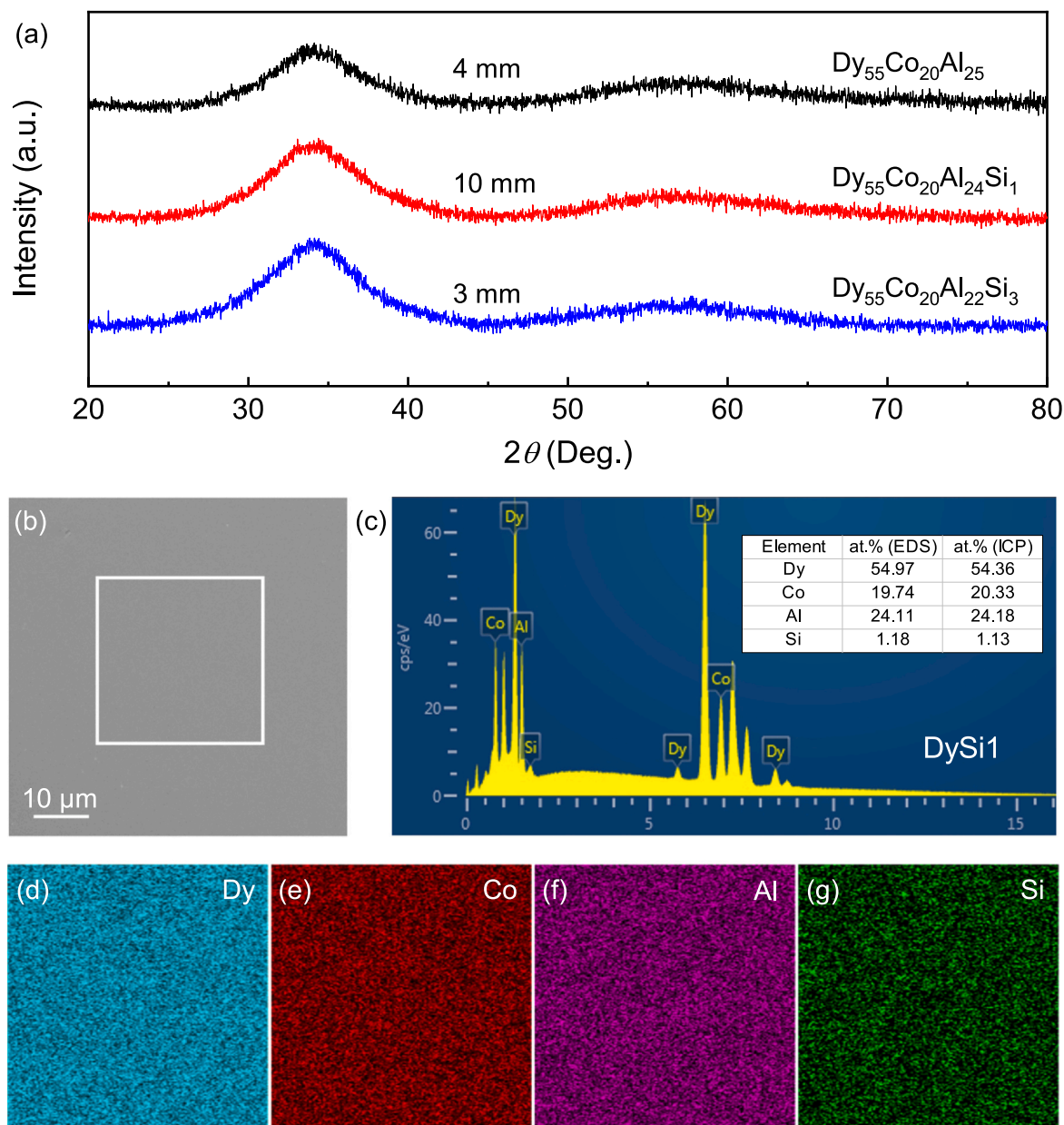


Fig. 1. (a) XRD patterns of $\text{Dy}_{55}\text{Co}_{20}\text{Al}_{25-x}\text{Si}_x$ ($x = 0, 1, 3$) BMG samples with the critical diameter. (b) SEM image of the DySi1 BMG sample. (c) EDS spectrum of the selected area in (b) with a size of $30 \times 30 \mu\text{m}^2$. The inserted table lists the final composition of the DySi1 BMG obtained by EDS and ICP. (d)-(g) Distributions of the Dy, Co, Al and Si elements in the corresponding region.

temperature of three fourth of the first crystallization peak. Combining small angle X-ray scattering measurement (SAXS) and transmission electron microscopy (TEM) observation, the development of precipitates with the prolongation of annealing time were investigated. Besides, thermodynamic and kinetic characterizations on base of driving force for crystallization and fragility of supercooled liquid were performed to elucidate the physical origin of the different crystallization behavior induced by Si addition.

2. Materials and methods

Master alloy ingots with nominal compositions of $\text{Dy}_{55}\text{Co}_{20}\text{Al}_{25-x}\text{Si}_x$ ($x = 0, 1, 3$) were prepared by arc melting a mixture of pure metals with a mass of 20 g under high-purity argon atmosphere. The purity of Dy is more than 99.9 wt%, and those for Co, Al and Si are no less than 99.99 wt%. Before melting the metals, Ti ingot was melted for five minutes to eliminate the remaining oxygen. Each ingot was re-melted for five times to ensure chemical homogeneity. The mass loss of the master alloy ingot after arc melting is less than 0.01 g (0.05 wt%). Then, copper mold casting method was used to fabricate BMG samples with different diameters. The final compositions of the prepared BMGs were identified by scanning electron microscope (SEM, Sirion 200, FEI) equipped with energy dispersive spectrometer (EDS) and inductively coupled plasma-atomic emission spectrometry (ICP-OES, ARCOS II, SPECTRO). The structure features of samples were characterized by X-ray diffraction (XRD, D8 Discover, Bruker), small-angle X-ray scattering (SAXS point 2.0, Anton Paar) and transmission electron microscope (TEM, Tecnai G20, FEI). The specimens for TEM observation were prepared by mechanical polishing and Ar ion milling (PIPS 691, Gatan) at 3.0 keV cooled by liquid nitrogen. Amorphous ribbons with a thickness of 15 μm were used for SAXS characterization. Thermal analyses were performed on differential scanning calorimeter (DSC, 404 F3, Netzsch), and the onset temperatures of glass transition (T_g), of crystallization (T_x), of melting (T_m) and the end temperature of glass transition (T_g^{end}) were determined using the tangent construction method. Isothermal crystallization kinetics of BMG samples were performed on DSC (DSC 8500, Perkin Elmer). BMG samples were heated to temperature of $T_g^{\text{end}} + 5\text{K}$ with a heating rate of 500 K/min, then isothermal annealed until complete crystallization. The annealing treatment was carried out on an annealing furnace under a vacuum of 10^{-4} Pa. Besides, specific heat capacity (C_p) and viscosity of alloys were measured to conduct thermodynamic and kinetic analyses. The detailed process of C_p measurement refers to Ref. [13,28], and that of viscosity measurement were listed in Ref. [13].

3. Results and discussion

3.1. Glass-forming ability

According to the reported results [29], the d_c of $\text{Dy}_{55}\text{Co}_{20}\text{Al}_{25}$ BMG was 3 mm. In this study, the corresponding d_c was ascertained to be 4 mm, which is slightly higher than the reported results. Fig. 1(a) shows the XRD patterns of the studied Dy-based BMG samples with the critical diameter. Only two broad diffusion humps without any crystalline peak can be detected for the samples, identifying their amorphous structures. It is noteworthy that the d_c of $\text{Dy}_{55}\text{Co}_{20}\text{Al}_{25}$ BMG is improved to 10 mm with 1 at% Si addition, respectively. This value is larger than the d_c of most ternary Hf-Co-Al BMGs. Since the vapor pressure of Dy is higher than that of Al, Al may be lost in arc melting. Therefore, SEM-EDS and ICP analyses were performed to identify the final chemical composition of the

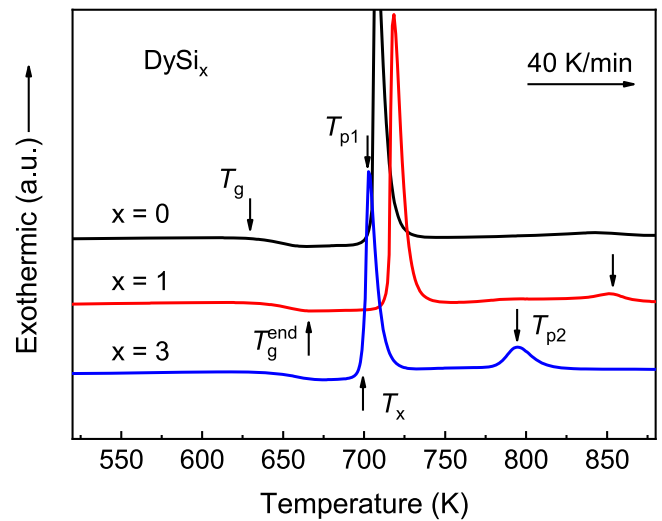


Fig. 2. DSC traces of DySix BMG samples with a heating rate of 40 K/min.

prepared BMG. Both the compositions obtained by EDS and ICP are consistent with the normal composition as listed in Fig. 1(c). Besides, all of the elements distribute homogeneously as shown in Fig. 1(d)–(g), which guarantees the repeatability of microalloying Si to improve the GFA of DyCoAl BMG. Hereafter, $\text{Dy}_{55}\text{Co}_{20}\text{Al}_{25-x}\text{Si}_x$ are denoted as DySix.

Fig. 2 shows the DSC traces of DySix ($x = 0, 1, 3$) BMG samples with a diameter of 2 mm under the heating rate of 40 K/min. It is seen that the T_g moves to higher temperature with the increase of Si content, but the T_x decreases with 3 at% Si addition. Thus, the largest value of supercooled liquid region (SCLR) is obtained in DySi1 BMG, indicating the best thermal stability of the SCLR for DySi1 BMG. The DySi3 BMG exhibits the narrowest SCLR of 58 K, which is consistent with its smallest d_c of 3 mm as shown in Fig. 1(a), and hint the lowest thermal stability of SCLR. Besides, a weak crystalline peak behind the first crystalline peak is observed in the DSC traces of Si-doped BMG samples, implying some new crystalline phases are induced by Si addition, which can affect the crystallization behavior of BMGs.

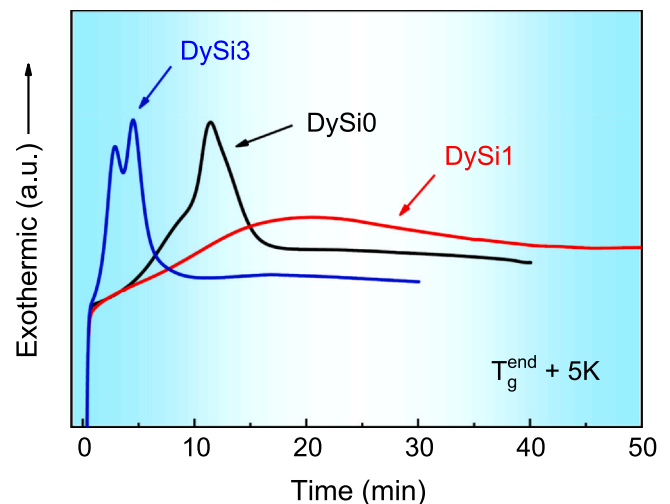


Fig. 3. Isothermal crystallization curves at the temperature of $T_g^{\text{end}} + 5\text{K}$ for DySix BMG samples.

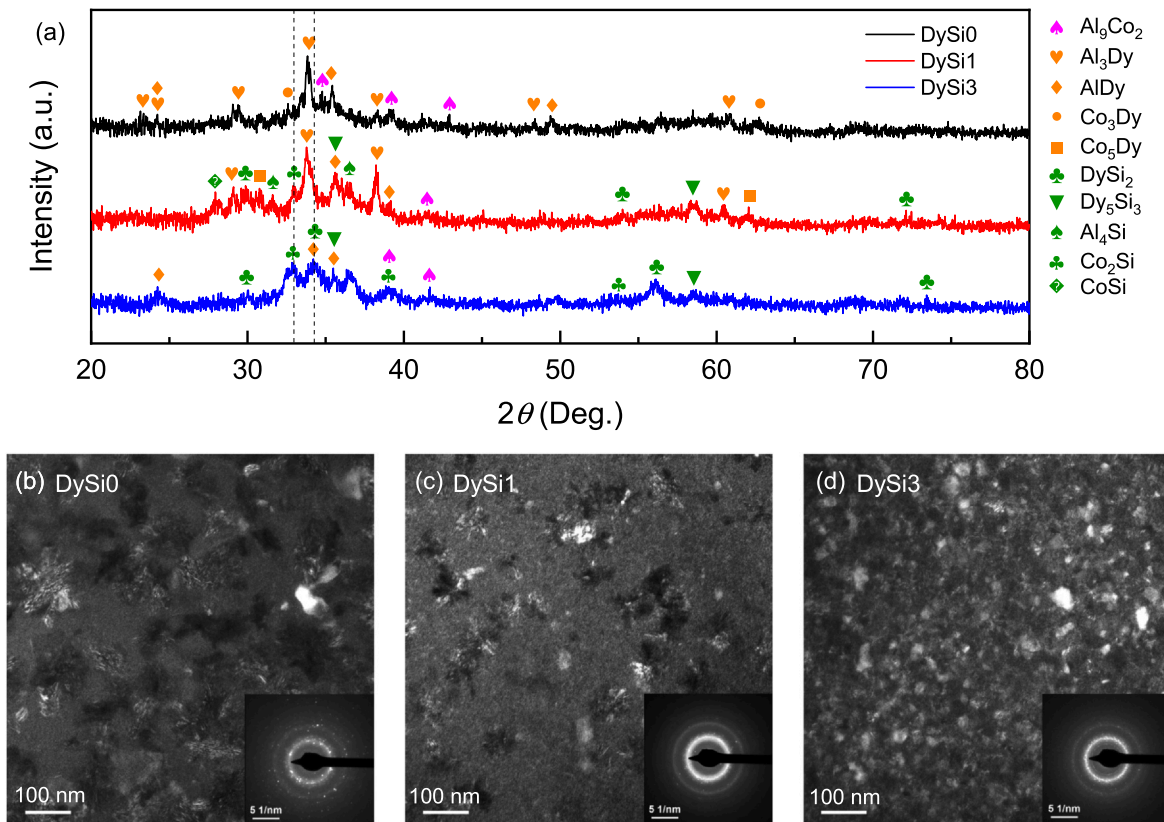


Fig. 4. (a) XRD patterns and (b)-(d) corresponding dark field TEM images for DySix BMG samples annealed at the temperature just over the first crystallization peak.

3.2. Effect of Si addition on crystallization behavior of BMG

To further explore the crystallization behaviors of DySix BMGs. Isothermal annealing at $T_g^{end} + 5K$ was carried out using DSC, with the curves shown in Fig. 3. It is clear that DySi1 sample possesses the longest incubation time and most sluggish crystallization process, while both the values decrease obviously with 3 at% Si addition. Particularly, two crystalline peaks are observed in the crystallization curve of DySi3 sample. It means that at least two crystalline phases precipitate successively in the isothermal process of DySi3 BMG sample. However, only single exothermic peak is detected for DySi0 and DySi1 samples, implying that Si addition alters the crystalline phases of BMGs.

The analyses of crystallization phases were performed by delicate heat treatment. In order to study the crystalline phases at the first crystallization peak of BMG samples, the as-cast samples were heated to the temperature of three fourth of the first crystallization peak with a heating rate of 20 K/min, i.e., 706, 712 and 700 K for DySi0, DySi1 and DySi3 samples, respectively, and then cooled down to room temperature immediately. The XRD patterns and corresponding TEM images are shown in Fig. 4. Due to the incomplete crystallization, partial diffusion humps preserve in the XRD patterns. For DySi0 sample, several phases including Al_3Dy , $AlDy$, Co_3Dy and Al_9Co_2 precipitate simultaneously at the first crystallization peak. The type of crystalline phases is consistent with the results of TbY-CoAl BMG [17]. With Si addition, other than the crystalline phases in DySi0 sample, some Si-containing phases such as $DySi_2$, Dy_5Si_3 and

Co_2Si etc. also precipitate at the first crystalline peak. Compared with DySi1 sample, the proportion of Si-containing phases for DySi3 sample is larger. From the dark field TEM images in Fig. 4(b)-(d), we can clearly see the variation of crystallization process with the increase of Si content. The size and fraction of crystalline phases decrease with 1 at% Si addition. Besides, obvious amorphous halos remain in the selected area electron diffraction (SAED) pattern of DySi1 sample, while that of DySi0 sample shows much more crystalline spots, which further identifies the suppression of crystallization with minor Si addition. However, an explosive nucleation is observed in DySi3 sample as shown in Fig. 4(d). Crystalline phases occupy almost the whole region, which means the crystallization resistance decreases with excessive Si addition.

Based on the above analyses, the evolution of crystallization process with different Si content can be proposed as normal nucleation (without Si addition), suppressed nucleation (minor Si addition) and explosive nucleation (excessive Si addition). When the content of Si is appropriate, the competition between Si-containing phases and initial Si-free phases lead to the frustration of crystallization. Under this condition, the Si-containing phases act as obstacles in the development of crystallization. On the contrary, with excessive Si addition, the large negative enthalpy of mixing between Si and other elements induces the preferential precipitation of Si-containing phases such as $DySi_2$. Thus, the incubation time decreases as shown in Fig. 3. Meanwhile, these preferentially precipitated phases lead to the reduction of Si concentration in the matrix, which promotes the precipitation of Si-free phases. Besides, the Si-

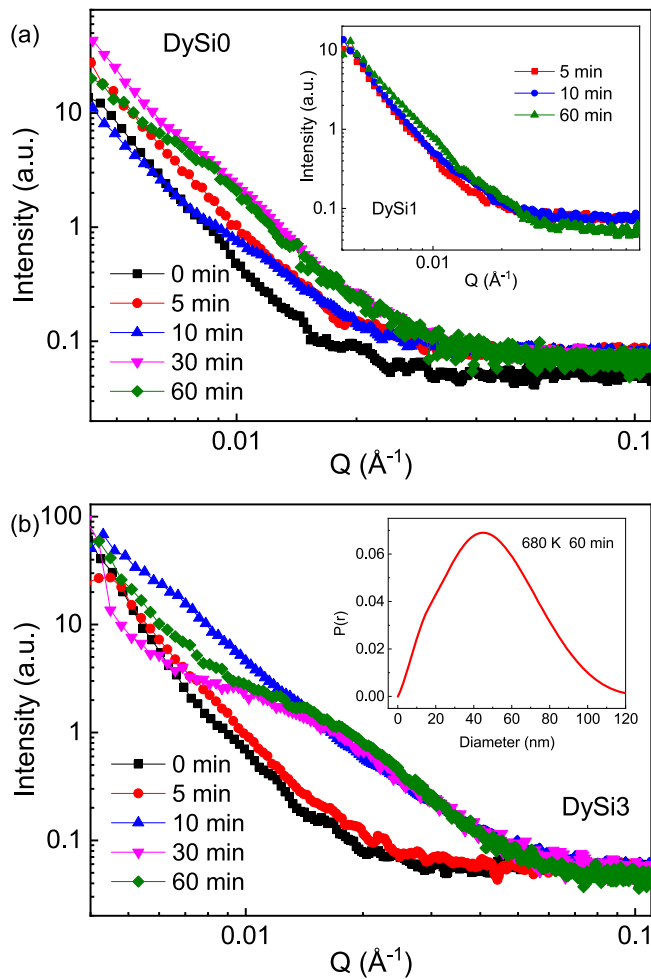


Fig. 5. SAXS profiles of DySix glassy ribbons upon isothermal annealing at the temperature of $T_g^{ind} + 10\text{K}$ depending on the annealing time, i.e., 670, 673 and 680 K for DySi0, DySi1 and DySi3 samples, respectively. Inset of (b) shows the volume distribution of the crystalline particles in the amorphous matrix after isothermal annealing at 680 K for 60 min.

containing phases can act as heterogeneous nucleation sites, which also accelerates the crystallization process. As a result, an explosive nucleation is observed as shown in Fig. 4(d).

Isothermal crystallization at SCLR with different annealing time were carried out to study the time dependence of crystallization for DySix MGs. Amorphous ribbons were heated to the target temperature (670, 673 and 680 K for DySi0, DySi1 and DySi3 samples, respectively) in an annealing furnace at high vacuum, then isothermally annealed for 5, 10, 30 and 60 min, respectively. The as-cast and annealed samples were then studied by SAXS and the profiles are shown in Fig. 5. The profile shows initially no scattering, and the overall intensity increases and an interference maximum appears with increasing annealing time. The interference maximum results from the simultaneous crystallization of multiple phases [30]. It can be seen that a shoulder occurs at 10 min and shifts to lower Q with the increase of annealing time for DySi0 sample, which agrees with the results reported by Wang et al. [31] and Liu et al. [32]. In contrast, the profile for DySi1 develops slowly. No evident shoulder can be observed even after annealing for 60 min as

shown in the inset of Fig. 5(a), indicating a sluggish crystallization. However, one can see that the shoulders are more evident at 30 and 60 min for DySi3 sample than those of DySi0 sample, corresponding to an accelerated crystallization. The real space pair distance distribution function $P(r)$ or PDDF can be obtained using a GIFT software [33]. A representative size distribution of the crystalline precipitates in the amorphous matrix for DySi3 sample is shown in the inset of Fig. 5(b). The result will be analyzed by combining the TEM observation in the following section.

The microstructures of the above crystalline samples were observed by TEM. Fig. 6 shows the dark field TEM images, and the insets are the corresponding SAED patterns. For the DySi0 sample annealed for 5 min, the SAED pattern exhibits several weak rings but no obvious diffraction spot is found, indicating the existence of a finely dispersed nanocrystals with random orientations. The TEM image in Fig. 6(a) containing nanocrystals with a size of 5–10 nm identifies this. With the increase of annealing time, the size and fraction of crystal increase as shown in Fig. 6(b)–(d). However, the DySi1 sample remains amorphous structure and displays a typical halo-like SEAD pattern after 5 min annealing. Although the initial precipitates are observed at 10 min as marked by yellow triangle in Fig. 6(f), no diffraction spots can be found in the SAED pattern, further confirming the sluggish crystallization of the DySi1 MG. Even after 60 min annealing, the size of crystals is relatively small and a large amount of amorphous matrix is preserved. Different from DySi1, the crystallization process is accelerated with 3 at% Si addition. As shown in Fig. 6(i)–(l), a great number of nanocrystals precipitate in the amorphous matrix after 5 min annealing, then propagate and grow rapidly. When the annealing time exceed 30 min, no obvious amorphous region can be observed, which is consistent with the pronounced scattering shoulders of SAXS profiles for the DySi3 sample as shown in Fig. 5(b).

According to the TEM image, the size distribution of the crystalline phases can be obtained [34]. For example, the distribution map of DySi1 sample annealed for 60 min is exhibited in the inset of Fig. 7. Gauss function is used to fit the data, and the mean size of crystalline particles is identified as 19.9 ± 0.4 nm. Similarly, the annealing time dependence of crystal size for DySi0, DySi1 and DySi3 samples are calculated and shown in Fig. 7. It is clear that the crystal size of DySi1 is smaller than those of DySi0 and DySi3 at the same annealing time, and the growth of crystal for DySi1 is more sluggish with the prolongation of annealing time. Besides, the crystalline particle size obtained from SAXS is also attached for comparison, which is consistent well with the TEM results.

3.3. Thermodynamic and kinetic analyses

Crystallization is controlled by the interplay of thermodynamics and kinetics. To elucidate the thermodynamic and kinetic origin of the distinctive crystallization behavior for MG samples with different Si content, two aspects including driving force for crystallization and fragility of SCL were studied. It is known that C_p plays an important role in the thermodynamic framework. Here, we measured the C_p data for crystal, glass and liquid using a temperature step method, as shown in Fig. 8(a)–(c) for DySi0, DySi1 and DySi3 samples, respectively. A typical C_p step corresponding to glass transition can be observed. The temperature dependences of C_p for liquids ($C_p^l(T)$) including SCL and stable liquid and crystal ($C_p^x(T)$) are fitted by the following equations respectively [35]:

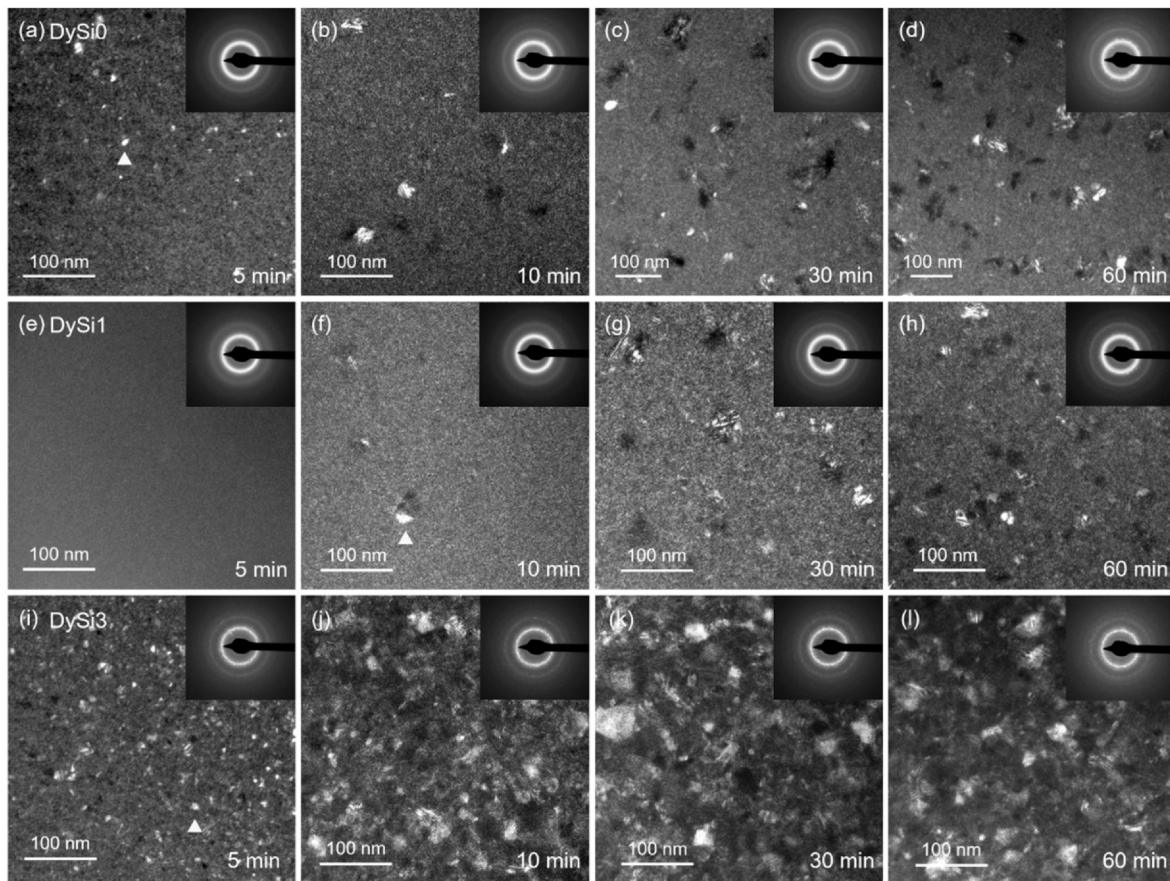


Fig. 6. Dark field TEM images and corresponding SAED patterns of glassy ribbons upon isothermal annealing at the temperature of $T_g^{end} + 10K$ depending on the annealing time for (a)-(d) DySi0, (e)-(h) DySi1 and (i)-(l) DySi3 samples.

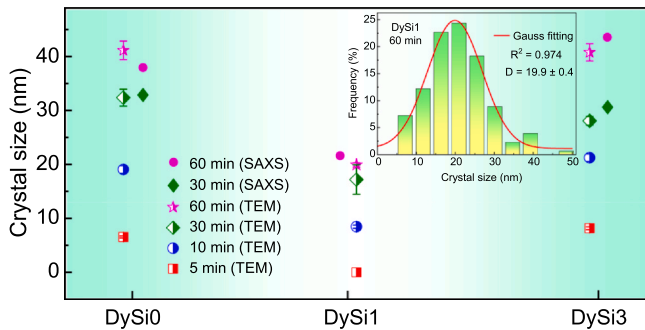


Fig. 7. Comparison of the crystal size for DySix MGs after annealing for various times at the temperature of $T_g^{end} + 10K$. The half-filled symbols are obtained from TEM observation and the filled symbols are calculated based on SAXS profiles. Inset shows the calculation of crystal size from the corresponding TEM images in Fig. 6(h).

$$C_p^l(T) = 3R + aT + bT^{-2} \quad (1)$$

$$C_p^x(T) = 3R + cT + dT^2 \quad (2)$$

where, R is the universal gas constant, a , b , c and d are fitting constants. Furthermore, combining the fitting data and enthalpy (ΔH_m)

and entropy (ΔS_m) of fusion as listed in Table 1, the Gibbs free energy difference between liquid and crystal (ΔG^{l-x}) can be calculated [36]. Fig. 8(d) shows the $\Delta G^{l-x}(T)$ curves for DySix alloys. As the driving force for crystallization is always connected with the degree of undercooling, the temperature axis is normalization by T_m for comparison of the driving forces between the alloys. At the same reduced temperature, the value of $\Delta G^{l-x}(T)$ for DySi0 is larger than that for DySi1, but smaller than that for DySi3, indicating the crystallization resistance of SCL is enhanced by proper Si addition, but reduced with excessive Si addition.

Other than thermodynamic considerations, the viscosity of the liquid is a key kinetic parameter that determines the crystallization of MGs. To obtain the viscosity of SCL, linear thermal expansion analyses of DySix BMG samples were performed on a TMA, and the curves are shown in Fig. 9(a). Below T_g , the linear thermal expansion coefficients keep almost unchanged for all of the samples. Subsequently, a contraction corresponding to glass transition is detected. After complete crystallization, samples expand again. Viscosity of SCL is calculated according to $\eta = \sigma/3\dot{\epsilon}$ [37], as shown in Fig. 9(b). In SCLR, viscosity decreases dramatically and the DySi1 sample possesses the widest SCLR and highest T_x , which is consistent with the DSC traces in Fig. 2. At the same temperature, the value of viscosity increases with the increase of Si addition. However, because of the distinction of characteristic temperature such as T_g , it is inadequate to describe the SCL just considering the value of viscosity. Kinetic

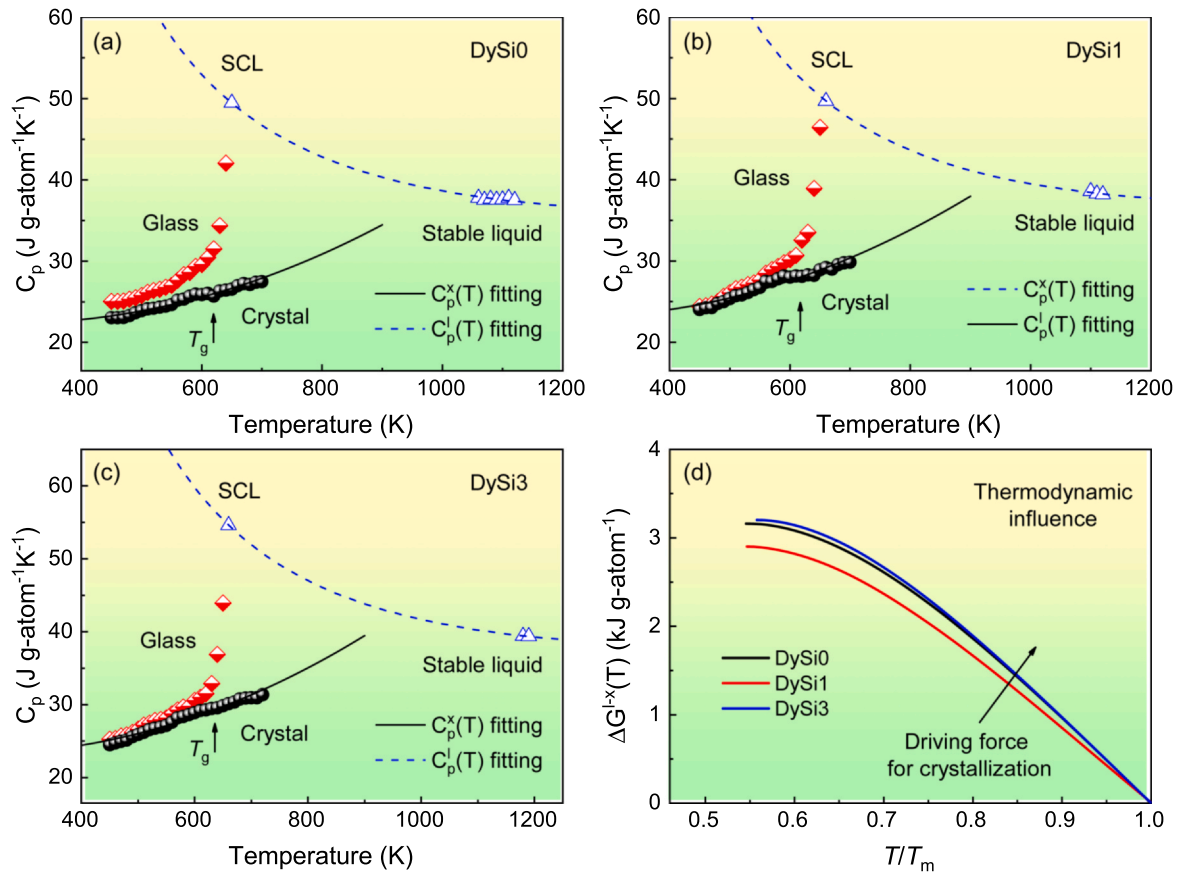


Fig. 8. C_p data of crystal (filled circles), glass (half-filled diamonds) and liquid (unfilled triangles) for (a) DySi0, (b) DySi1 and (c) DySi3 samples. (d) Temperature dependence of Gibbs free energy difference (ΔG^{l-x}) for DySix alloys, the temperature axis is normalized by T_m .

fragility based on the temperature dependence of viscosity is a common parameter to depict SCL [38,39]. Fig. 10(a) shows the Angell plots of the measured viscosity. The viscosity is plotted logarithmically over the inverse temperature nominated by the glass transition temperature, and fitted by Vogel-Fulcher-Tammann (VFT) relation [40]:

$$\eta(T) = \eta_0 \exp\left(\frac{D^* \cdot T_0}{T - T_0}\right) \quad (3)$$

where η_0 is the lowest possible viscosity in the high temperature liquid state, D^* and T_0 are the fragility parameter and VFT temperature, respectively. It is seen that the curve of DySi1 sample locates above those of DySi0 and DySi3 samples, quantified by the largest value of D^* as listed in the table of Fig. 10(a). This means the SCL changes from fragile to strong with minor Si addition, but turns to fragile again with excessive Si addition.

Table 1

Overview of thermophysical properties including T_g , T_g^{end} and T_x determined from DSC traces under the heating rate of 40 K/min, and T_m , ΔH_m and ΔS_m under the heating rate of 20 K/min, as well as fitting parameters for the C_p data obtained from Eqs. (1) and (2) for DySi0, DySi1 and DySi3 BMGs.

Composition	T_g (K)	T_g^{end} (K)	T_x (K)	T_m (K)	ΔH_m (kJ g-atom ⁻¹)	ΔS_m (J g-atom ⁻¹ K ⁻¹)	a	b	c	d
DySi0	632	660	705	1000	9.75	9.75	0.00462	9.08×10^6	-0.0180	3.18×10^{-5}
DySi1	636	664	715	1013	8.35	8.24	0.00531	9.25×10^6	-0.0158	3.36×10^{-5}
DySi3	642	670	700	1007	9.63	8.55	0.00534	1.14×10^7	-0.0153	3.48×10^{-5}

According to the Adam-Gibbs theory [41], fragility is associated with the temperature dependence of configuration entropy (S_c) as described by Eq. (4):

$$\eta(T) = \eta_0 \exp\left(\frac{C}{TS_c(T)}\right) \quad (4)$$

where the constant C is proportional to the free energy barrier for a cooperative rearrangement. $S_c(T)$ can be expressed as [42]:

$$S_c(T) = S_c(T_m^*) + \int_{T_m}^T \frac{\Delta C_p^{l-x}(T')}{T'} dT' \quad (5)$$

where $S_c(T_m^*)$ is the configurational entropy at a fixed viscosity value of 1 Pa. Thus, $\Delta C_p^{l-x}(T)/T$ can describe the changing rate of the $S_c(T)$ approaching T_g . It was pointed out that Eq. (5) requires the assumption that the vibrational contribution to the total entropy changes with the same rate [42,43]. As shown in Fig. 9(a), below T_g ,

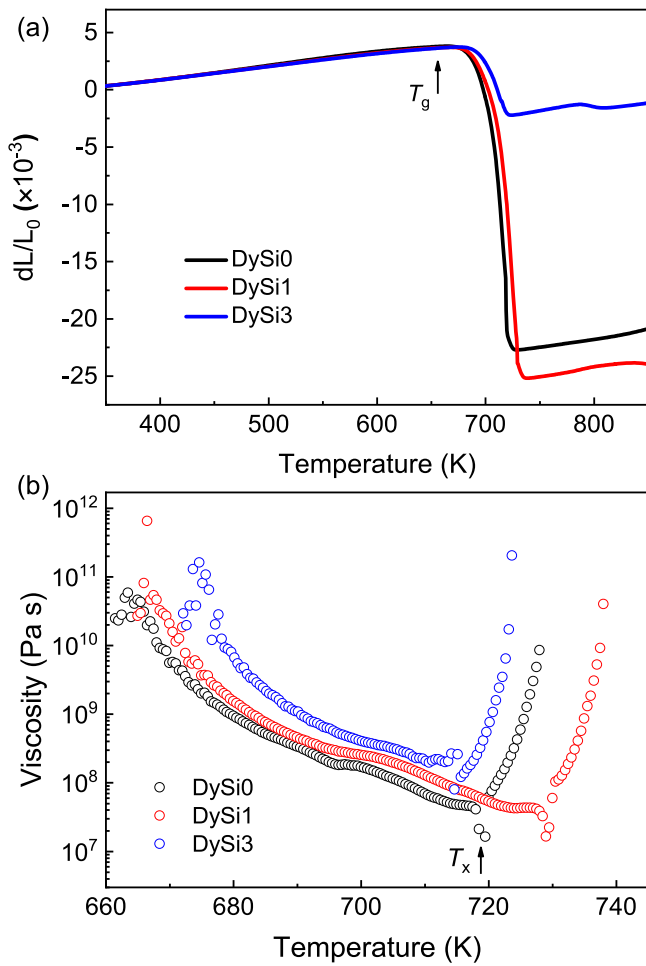


Fig. 9. (a) TMA traces and (b) viscosity of the supercooled liquid for DySix BMG samples.

the linear thermal expansion coefficients keep almost unchanged for all of the samples, indicating an alike contribution of vibration to the total entropy [44], which results in a similar proportionality factor between the excessive entropy and the configurational entropy. Therefore, in this study $\Delta C_p^{l-x}(T)/T$ can reflect the fragility of the DySix SCL. As shown in Fig. 10(b), the variation of D^* obtained from $\Delta C_p^{l-x}(T)/T$ is consistent with the result of Angell plots, i.e., the DySi1 sample shows the strongest SCL behavior.

In the classical nucleation theory [45], the free energy cost of crystal nucleation at the top of the nucleation barrier ΔG^* can be expressed as $\Delta G^* = 16\pi\gamma_{l-x}^3/3(\Delta G^{l-x})^2$, where γ_{l-x} denotes the interface tension between liquid and crystal. For a given γ_{l-x} , ΔG^* increases with the decrease of ΔG^{l-x} . The nucleation time is given by $\tau_n(T) = K \exp(\Delta G^*/RT)$, where R is the universal gas constant and K is a kinetic prefactor proportional to the characteristic time of material transport controlling crystallization, namely the inverse of the diffusion coefficient D^{-1} . Generally, the viscosity can be inversely connected by Stokes-Einstein equation to the diffusion coefficient, i.e., $D \propto \eta^{-1}$ [46]. According to the above analyses, microalloying Si element leads to low ΔG^{l-x} and high viscosity of SCL, thus large ΔG^* and low D . This indicates that the alloy with minor Si addition possesses high free energy against crystallization and low atomic mobility, while excessive Si addition leads to reverse variation. Therefore, the sluggish crystallization of the DySi1 BMG attributes to the combination of low driving force for crystallization and strong SCL behavior.

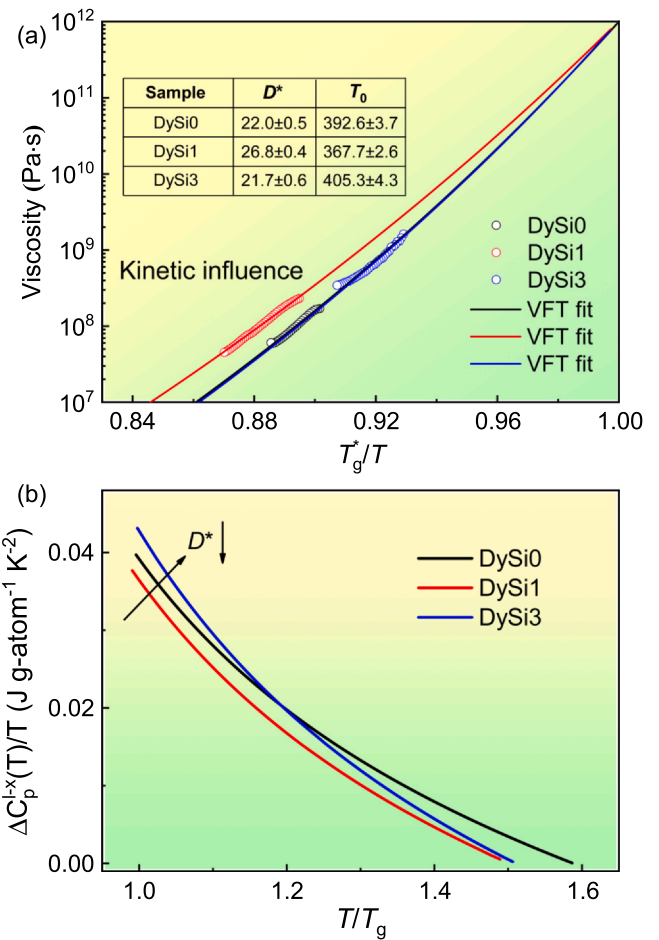


Fig. 10. (a) Angell plots for DySix alloys, corresponding parameters of VFT fitting are listed in the inserted table. (b) Rate of excess entropy change for DySix BMGs as a function of the T_g -scaled temperature.

4. Conclusion

In summary, the glass-forming ability of DyCoAl BMG was improved by more than two times with 1 at% Si addition. Centimeter-level Dy₅₅Co₂₀Al₂₄Si₁ BMG was prepared. The BMG samples with different Si content show distinctive crystallization behaviors. Microalloying Si induces the Si-containing phases such as DySi₂ and Dy₅Si₃ precipitate simultaneously with the Si-free phases at the initial crystallization stage. Compared with the non-Si BMG, the crystallization process transforms to a suppressed nucleation with minor Si addition then to an explosive nucleation with excessive Si addition. Besides, the crystalline particles grow sluggishly for DySi1 BMG whereas develop rapidly to complete crystallization for DySi3 BMG. Thermodynamic and kinetic analyses indicate that the alloy with minor Si addition possesses low driving force for crystallization and strong supercooled liquid behavior while excessive Si addition leads to reverse variations, which accounts for the distinctive crystallization behaviors of BMGs with different Si content. This work clarifies the crystallization characteristics of Dy-based BMGs with Si addition and provide underlying guidance to modulate the magnetocaloric properties of Dy-based BMGs by crystallization treatment.

CRediT authorship contribution statement

Liliang Shao: Methodology, Data curation, Investigation, Writing - original draft. **Lin Xue:** Investigation. **Qianqian Wang:** Writing -

review & editing. **Kaili Ma:** Investigation. **Jindu Huang:** Investigation. **Baolong Shen:** Conceptualization, Methodology, Funding acquisition, Project administration, Supervision, Writing - review & editing.

Declaration of Competing Interest

The authors declare no conflict of interest.

Acknowledgements

This work was supported by the National Natural Science Foundation of China (Grant No. 51631003), the Natural Science Foundation of Jiangsu Province of China (Grant No. BK20191269), and the Fundamental Research Funds for the Central Universities (Grant No. 2242019k1G005).

References

- V.K. Pecharsky, K.A. Gschneidner Jr., Giant magnetocaloric effect in $Gd_5(Si_2Ge_2)$, *Phys. Rev. Lett.* 78 (1997) 4494–4497, <https://doi.org/10.1103/PhysRevLett.78.4494>
- K.A. Gschneidner Jr., V.K. Pecharsky, Magnetocaloric materials, *Annu. Rev. Mater. Sci.* 30 (2000) 387–429, <https://doi.org/10.1146/annurev.matsci.30.1.387>
- A. Kitanovski, P.W. Egolf, Thermodynamics of magnetic refrigeration, *Int. J. Refrig.* 29 (2006) 3–21, <https://doi.org/10.1016/j.ijrefrig.2005.04.007>
- V. Franco, J.S. Blazquez, J.J. Ipus, J.Y. Law, L.M. Moreno-Ramirez, A. Conde, Magnetocaloric effect: from materials research to refrigeration devices, *Prog. Mater. Sci.* 93 (2018) 112–232, <https://doi.org/10.1016/j.pmatsci.2017.10.005>
- Q. Luo, D.Q. Zhao, M.X. Pan, W.H. Wang, Magnetocaloric effect of Ho-, Dy-, and Er-based bulk metallic glasses in helium and hydrogen liquefaction temperature range, *Appl. Phys. Lett.* 90 (2007) 211903, <https://doi.org/10.1063/1.2741120>
- Q. Luo, W.H. Wang, Rare earth based bulk metallic glasses, *J. Non-Cryst. Solids* 355 (2009) 759–775, <https://doi.org/10.1016/j.jnoncrysol.2009.02.006>
- F. Yuan, J. Du, B.L. Shen, Controllable spin-glass behavior and large magnetocaloric effect in Gd-Ni-Al bulk metallic glasses, *Appl. Phys. Lett.* 101 (2012) 032405, <https://doi.org/10.1063/1.4738778>
- L. Xia, Q. Guan, D. Ding, M.B. Tang, Y.D. Dong, Magneto-caloric response of the $Gd_{60}Co_{25}Al_{15}$ metallic glasses, *Appl. Phys. Lett.* 105 (2014) 192402, <https://doi.org/10.1063/1.4901263>
- J.T. Huo, L.S. Huo, H. Men, X.M. Wang, A. Inoue, J.Q. Wang, C.T. Chang, R.W. Li, The magnetocaloric effect of Gd-Tb-Dy-Al-M (M = Fe, Co and Ni) high-entropy bulk metallic glasses, *Intermetallics* 58 (2015) 31–35, <https://doi.org/10.1016/j.intermet.2014.11.004>
- Q. Luo, W.H. Wang, Magnetocaloric effect in rare earth-based bulk metallic glasses, *J. Alloy Compd.* 495 (2010) 209–216, <https://doi.org/10.1016/j.jallcom.2010.01.125>
- H. Fu, M. Zou, Magnetic and magnetocaloric properties of ternary Gd-Co-Al bulk metallic glasses, *J. Alloy Compd.* 509 (2011) 4613–4616, <https://doi.org/10.1016/j.jallcom.2011.01.126>
- V. Franco, J.S. Blazquez, C.F. Conde, A. Conde, A Finemet-type alloy as a low-cost candidate for high-temperature magnetic refrigeration, *Appl. Phys. Lett.* 88 (2006) 042505, <https://doi.org/10.1063/1.2167803>
- L.L. Shao, L. Xue, Q. Luo, Q.Q. Wang, B.L. Shen, The role of Co/Al ratio in glass-forming GdCoAl magnetocaloric metallic glasses, *Materialia* 7 (2019) 100419, <https://doi.org/10.1016/j.mtla.2019.100419>
- L.L. Zhang, M.D. Bao, Q. Zheng, L.H. Tian, J. Du, Magnetocaloric effect in high Gd content Gd-Fe-Al based amorphous/nanocrystalline systems with enhanced Curie temperature and refrigeration capacity, *AIP Adv.* 6 (2016) 035220, <https://doi.org/10.1063/1.4945407>
- Q. Zheng, L.L. Zhang, J. Du, Magnetic entropy change in $Gd_{95}Fe_{2.8}Al_{2.2}$ amorphous/nanocrystalline ribbons, *Scr. Mater.* 130 (2017) 170–173, <https://doi.org/10.1016/j.scriptamat.2016.11.041>
- X.C. Zhong, H.Y. Mo, X.W. Huang, X.Y. Shen, X.L. Feng, D.L. Jiao, Z.W. Liu, Effects of crystallization treatment on the structure and magnetic properties of $Gd_{65}Fe_{25}Zn_{10}$ alloy ribbons for magnetic, *J. Alloy Compd.* 730 (2018) 493–500, <https://doi.org/10.1016/j.jallcom.2017.09.321>
- Q. Luo, B. Schwarz, N. Mattern, J. Shen, J. Eckert, Roles of hydrogenation, annealing and field in the structure and magnetic entropy change of Tb-based bulk metallic glasses, *AIP Adv.* 3 (2013) 032134, <https://doi.org/10.1063/1.4797619>
- H. Fu, Z. Ma, X.J. Zhang, D.H. Wang, B.H. Teng, E.A. Balfour, Table-like magnetocaloric effect in the Gd-Co-Al alloys with multi-phase structure, *Appl. Phys. Lett.* 104 (2014) 072401, <https://doi.org/10.1063/1.4865554>
- S. Li, X.K. Xi, W. Wei, Q. Luo, Y.T. Wang, M.B. Tang, B. Zhang, Z.F. Zhao, R.J. Wang, M.X. Pan, D.Q. Zhao, W.H. Wang, Formation and properties of new heavy rare-earth-based bulk metallic glasses, *Sci. Technol. Adv. Mat.* 6 (2005) 823–827, <https://doi.org/10.1016/j.stam.2005.06.019>
- L. Xue, J. Li, W.M. Yang, C.C. Yuan, B.L. Shen, Effect of Fe substitution on magnetocaloric effects and glass-forming ability in Gd-based metallic glasses, *Intermetallics* 93 (2018) 67–71, <https://doi.org/10.1016/j.intermet.2017.11.007>
- W.H. Wang, Roles of minor additions in formation and properties of bulk metallic glasses, *Prog. Mater. Sci.* 52 (2007) 540–596, <https://doi.org/10.1016/j.pmatsci.2006.07.003>
- F.A. de Lucena, C.S. Kiminami, C.R.M. Afonso, New compositions of Fe-Co-Nb-B-Y BMG with wide supercooled liquid range, over 100 K, *J. Mater. Res. Technol.* 9 (2020) 9174–9181, <https://doi.org/10.1016/j.jmrt.2020.06.035>
- A. Takeuchi, A. Inoue, Classification of bulk metallic glasses by atomic size difference, heat of mixing and period of constituent elements and its application to characterization of the main alloying element, *Mater. Trans.* 46 (2005) 2817–2829, <https://doi.org/10.2320/matertrans.46.2817>
- Y.B. Zhao, Y.W. Bai, Y.J. Ding, L.N. Hu, Predicting the glass-forming ability of rare earth-contained Fe-based alloys by features of dynamic transition in their melts, *J. Non Cryst. Solids* 537 (2020) 120020, <https://doi.org/10.1016/j.jnoncrysol.2020.120020>
- X.K. Xi, L.L. Li, B. Zhang, W.H. Wang, Y. Wu, Correlation of atomic cluster symmetry and glass-forming ability of metallic glass, *Phys. Rev. Lett.* 99 (2007) 095501, <https://doi.org/10.1103/PhysRevLett.99.095501>
- L. Yang, G.Q. Guo, Structural origin of the high glass-forming ability in Gd doped bulk metallic glasses, *Appl. Phys. Lett.* 97 (2010) 091901, <https://doi.org/10.1063/1.3485117>
- Q. Wang, C.T. Liu, Y. Yang, J.B. Liu, Y.D. Dong, J. Lu, The atomic-scale mechanism for the enhanced glass-forming-ability of a Cu-Zr based bulk metallic glass with minor element additions, *Sci. Rep.* 4 (2014) 4648, <https://doi.org/10.1038/srep04648>
- I. Gallino, M.B. Shah, R. Busch, Enthalpy relaxation and its relation to the thermodynamics and crystallization of the $Zr_{78.5}Cu_{15.6}Ni_{12.8}Al_{10.3}Nb_{2.8}$ bulk metallic glass-forming alloy, *Acta Mater.* 55 (2007) 1367–1376, <https://doi.org/10.1016/j.actamat.2006.09.040>
- S. Li, R.J. Wang, M.X. Pan, D.Q. Zhao, W.H. Wang, Formation and properties of $RE_{55}Al_{25}Co_{20}$ (RE = Y, Ce, La, Pr, Nd, Gd, Tb, Dy, Ho and Er) bulk metallic glasses, *J. Non Cryst. Solids* 354 (2008) 1080–1088, <https://doi.org/10.1016/j.jnoncrysol.2007.08.022>
- J. Kim, H.S. Oh, J. Kim, C.W. Ryu, G.W. Lee, H.J. Chang, E.S. Park, Utilization of high entropy alloy characteristics in Er-Gd-Y-Al-Co high entropy bulk metallic glass, *Acta Mater.* 155 (2018) 350–361, <https://doi.org/10.1016/j.actamat.2018.06.024>
- X.L. Wang, J. Almer, C.T. Liu, Y.D. Wang, J.K. Zhao, A.D. Stoica, D.R. Haefliger, W.H. Wang, In situ synchrotron study of phase transformation behaviors in bulk metallic glass by simultaneous diffraction and small angle scattering, *Phys. Rev. Lett.* 91 (2003) 265501, <https://doi.org/10.1103/PhysRevLett.91.265501>
- X.J. Liu, X.D. Hui, G.L. Chen, M.H. Sun, In situ synchrotron SAXS study of nanocrystallization in $Zr_{65}Ni_{25}Ti_{10}$ metallic glass, *Intermetallics* 16 (2008) 10–15, <https://doi.org/10.1016/j.intermet.2007.06.014>
- X.L. Wu, S. Lan, Z.D. Wu, X.Y. Wei, Y. Ren, H.Y. Tsang, X.L. Wang, Multiscale structures of Zr-based binary metallic glasses and the correlation with glass forming ability, *Prog. Nat. Sci.* 27 (2017) 482–486, <https://doi.org/10.1016/j.pnsc.2017.08.008>
- L. Hou, X.D. Fan, Q.Q. Wang, W.M. Yang, B.L. Shen, Microstructure and soft-magnetic properties of FeCoPCu nanocrystalline alloys, *J. Mater. Sci. Technol.* 35 (2019) 1655–1661, <https://doi.org/10.1016/j.jmst.2019.03.030>
- O. Kubaschewski, C.B. Alcock, P.J. Spencer, *Materials Thermochemistry*, Pergamon Press, New York, 1993.
- R. Busch, Y.J. Kim, W.L. Johnson, Thermodynamics and kinetics of the ungercooled liquid and the glass-transition of the $Zr_{41.2}Ti_{13.8}Cu_{12.5}Ni_{10.0}Be_{22.5}$ alloy, *J. Appl. Phys.* 77 (1995) 4039–4043, <https://doi.org/10.1063/1.359485>
- N. Nishiyama, A. Inoue, Glass transition behavior and viscous flow working of $Pd_{40}Cu_{30}Ni_{10}P_{20}$ amorphous alloy, *Mater. Trans.* 40 (1999) 64–71, <https://doi.org/10.2320/matertrans1989.40.64>
- M.D. Ediger, C.A. Angell, S.R. Nagel, Supercooled liquids and glasses, *J. Phys. Chem.* 100 (1996) 13200–13212, <https://doi.org/10.1021/jp953538d>
- R. Busch, E. Bakke, W.L. Johnson, Viscosity of the supercooled liquid and relaxation at the glass transition of the $Zr_{46.75}Ti_{18.25}Cu_{7.5}Ni_{10}Be_{27.5}$ bulk metallic glass forming alloy, *Acta Mater.* 46 (1998) 4725–4732, [https://doi.org/10.1016/s1359-6454\(98\)00122-0](https://doi.org/10.1016/s1359-6454(98)00122-0)
- C.A. Angell, Formation of glasses from liquids and biopolymers, *Science* 267 (1995) 1924–1935, <https://doi.org/10.1126/science.267.5206.1924>
- G. Adam, J.H. Gibbs, On the temperature dependence of cooperative relaxation properties in glass-forming liquids, *J. Chem. Phys.* 43 (1965) 139–146, <https://doi.org/10.1063/1.1696442>
- I. Gallino, J. Schroers, R. Busch, Kinetic and thermodynamic studies of the fragility of bulk metallic glass forming liquids, *J. Appl. Phys.* 108 (2010) 063501, <https://doi.org/10.1063/1.3480805>
- P.G. Debenedetti, F.H. Stillinger, Supercooled liquids and the glass transition, *Nature* 410 (2001) 259–267, <https://doi.org/10.1038/35065704>
- M.Q. Jiang, M. Naderi, Y.J. Wang, M. Peterlechner, X.F. Liu, F. Zeng, F. Jiang, L.H. Dai, G. Wilde, Thermal expansion accompanying the glass-liquid transition and crystallization, *AIP Adv.* 5 (2015) 127133, <https://doi.org/10.1063/1.4939216>
- D. Turnbull, Under what conditions can a glass be formed, *Contemp. Phys.* 10 (1969) 473–488, <https://doi.org/10.1080/00107516908204405>
- F. Puosi, A. Pasturel, Nucleation kinetics in a supercooled metallic glass former, *Acta Mater.* 174 (2019) 387–397, <https://doi.org/10.1016/j.actamat.2019.05.057>